Applied Catalysis B: Environmental 183 (2016) 75–85

Contents lists available at ScienceDirect

Applied Catalysis B: Environmental

journal homepage: www.elsevier.com/locate/apcatb

Photoelectrocatalytic oxidation of bisphenol A over mesh of TiO_2/graphene/Cu_2O

Lixia Yang [a,b], Zhongyan Li [a,b], Huimin Jiang [a,b], Wenjing Jiang [a,b], Rongkui Su [a,b], Shenglian Luo [a,b,*], Yan Luo [a,b]

[a] High Level Laboratory of Jiangxi Province for Persistent Pollutants Control, Recycle and Reuse, Nanchang 330063, PR China
[b] Deparment of Environmental and Chemical Engineering, Nanchang Hangkong University, Nanchang 330063, PR China

ARTICLE INFO

Article history:
Received 10 May 2015
Received in revised form 19 August 2015
Accepted 12 October 2015
Available online 23 October 2015

Keywords:
TiO_2/graphene/Cu_2O mesh
Photocatalyst
Photoelectrocatalytic degradation
Bisphenol A

ABSTRACT

Mesh of TiO_2/graphene/Cu_2O was fabricated by chemical vapor deposition of graphene following electrochemical deposition of Cu_2O on anodized Ti soft wire bearing TiO_2 nanotubes. The mesh of TiO_2/graphene/Cu_2O was applied in photoelectrocatalytic oxidation of bisphenol A (BPA). The as-prepared TiO_2/graphene/Cu_2O mesh was used as both catalyst and electrode. Under visible light irradiation, BPA was effectively oxidized through photoelectrocatalysis over the TiO_2/graphene/Cu_2O mesh. Three main intermediates were evidenced during photoelectrocatalytic degradation of BPA, and no toxic products were determined. A detailed pathway of BPA degradation by TiO_2/G/Cu_2O is proposed based on the identified intermediates.

1. Introduction

Bisphenol A (2,2-bis(4-hydroxyphenyl) propane, BPA) is an organic chemical with various applications in the polymer industry. The global demand for BPA increased from 3.2 million tons in 2003 [1] to 5.5 million tons in 2011 [2]. With the extensive use of BPA, this compound has been detected at concentrations up to 21.5 $\mu g\,L^{-1}$ in urban wastewaters [3] and within the ranges of 1.92–11.1 $\mu g\,L^{-1}$ in industrial wastewater [4], 0.14–0.98 $\mu g\,L^{-1}$ in treated effluents [5], and 0.5–2 $\mu g\,L^{-1}$ in drinking water [6]. BPA has emerged as an environmental pollutant that causes diverse cellular responses even at low doses [7]. In particular, BPA acts as an endocrine disruptor [8–11]. The predicted no-effect concentration of BPA for aquatic wild life has been revised and decreased from 100 $\mu g\,L^{-1}$ to 0.06 $\mu g\,L^{-1}$ [12]. Several studies have reported that exposure to very low BPA levels affects humans and may result in reduced fertility and increased incidence of breast, ovarian, and testicular cancers. Elimination of even low BPA concentrations from water becomes an urgent issue from the viewpoint of environmental remediation and human health [13,14]. Moreover, BPA cannot be completely mineralized and its byproducts, which exhibit high endocrine-disrupting action, could be produced during the treatment process [15]. Thus, BPA must be completely transformed into CO_2 and removed from water.

Various methods, such as biological, chemical, electrochemical oxidation, and photocatalytic, have been developed to remove BPA from water [16–22]. As the most promising semiconductor catalyst, TiO_2 [23] and TiO_2-based [24] photocatalysts have been extensively investigated in the field of photocatalytic degradation. Given the difficulty of constructing solid-state, conductive semiconductor films, several reports documented that photoelectrocatalysis is an effective route to enhance photocatalytic degradation of BPA. In the last recent decade, anodic TiO_2 nanotube arrays grown on Ti substrate have been widely studied because of their superior advantages on constructing solid photocatalysts with high specific surface area and activity [25]. Taking TiO_2 nanotube arrays/Ti in photocatalysis can spare the operation of separating the photocatalyst in powder form from the treated water after degradation, which avoids the secondary pollution. In addition, one of the inherent outstanding advantages of anodic TiO_2 nanotube arrays/Ti is that it can be use both photocatalyst and electrode. As known, hole and electron are generated when TiO_2 is excited by the lights with their photoenergy being higher than the band gap of TiO_2. If the electrons and hoes immediately recombine, only heat is produced and the probability for desired redox reaction is lost. However, the recombination of hole and electron can be restrained through applying an external potential to the photocatalyst. Photoelectrocatalytic (PEC) degradation of organic pollutants has attracted great interest with

* *Corresponding author at: High Level Laboratory of Jiangxi Province for Persistent Pollutants Control, Recycle and Reuse, Nanchang Hangkong University, Nanchang 310063, PR China. Fax: +86 791 83953373.
E-mail address: sllou@hnu.edu.cn (S. Luo).

http://dx.doi.org/10.1016/j.apcatb.2015.10.023

TiO_2 films immobilized on conductive substrates [26–29]. Assisted by a bias potential, the working electrode is positively biased to the counter electrode, the photogenerated electrons in TiO_2 anode can be conducted to the external circuit. This is more efficient in the use of electrons and holes and thereby improves the final photocatalytic efficiency over photocatalysis [26–29].

In this work, highly ordered TiO_2 nanotubes were grown on soft Ti mesh which was weaved from Ti wires. The internal stress inside the anodic TiO_2 nanotubes grown on cylindrical Ti wires was lower than that on traditional Ti foils, thereby the physical stability of the long TiO_2 nanotubes grown on the Ti mesh are stronger than the one on traditional Ti foils. Then graphene was grown in situ on the TiO_2 nanotubes through chemical vapor deposition using Ni as a catalyst. As a highly conductive medium, graphene layers were formed on the external and inner walls of the nanotubes. Graphene was also formed in the space between two TiO_2 nanotubes, rendering the ordered TiO_2 nanotube arrays a conductive, integrated and immobilized electrode. To improve the response of the as-prepared TiO_2/graphene to visible light, we deposited Cu_2O particles to construct a ternary photocatalytic electrode designated as $TiO_2/G/Cu_2O$ mesh which was expected to be a stable photoanode in PEC system because of its good conductivity and integrity.

The $TiO_2/G/Cu_2O$ mesh was used as the photoelectrocatalyst to eliminate BPA from water. The influence of different factors, such as initial solution pH and bias potential were investigated. The photocatalytic and photoelectrocatalytic activities of the $TiO_2/G/Cu_2O$ mesh were compared. Intermediates generated during the degradation were identified and the decomposition pathway of BPA is proposed.

2. Experimental

2.1. Materials

Titanium wires (Φd = 0.6 mm, 99.6%) were purchased from Guangdong Zhengxiang Metal Material Limited Company, China. Dimethyl sulfoxide (DMSO), hydrogen fluoride (HF), nickel chloride ($NiCl_2$), copper sulfate pentahydrate ($CuSO_4\cdot 5H_2O$), sodium hydroxide (NaOH) and hydrochloric acid (HCl) were of analytical grade. Acetonitrile was of HPLC grade. All the other reagents were analytical grade purity, and were used as received without further purification. Milli-Q water was used throughout this study.

2.2. Fabrication of $TiO_2/G/Cu_2O$ mesh

2.2.1. TiO_2/G mesh

First, the titanium wires were weaved into a titanium mesh with a geometrical size of 1 cm × 5 cm (Fig. 1a) by using a mini knitter. Then the Ti mesh was anodized in a two-electrode configuration with a Ti mesh anode and a Pt foil cathode in a dimethyl sulfoxide solution containing 2 wt.% hydrofluoric acid at 40 V for 8 h. The as-fabricated TiO_2 nanotube arrays have an amorphous crystallographic structures. Upon annealing at elevated temperatures, the nanotubes can transform into anatase phase [25]. The titanium nanotubes (Fig. 1b) were then plated with nickel in 0.5 M $NiCl_2$ solution in three-electrode mode of the electrochemical workstation (CHI660C, Shanghai, China). The TiO_2/Ni specimen was placed in a graphite cell and added with poly(ethylene glycol) 6000 (PEG6000). The content of PEG6000 in the tube furnace was controlled at 300 mg/cm^3 to maintain the top of the TiO_2 nanotube open for further modification and application. Graphene layers were formed on the TiO_2 nanotubes by carbonizing PEG6000 at 600 °C for 6 h with a heating and cooling rate of 2 °C/min under N_2 atmosphere. The PEG6000 has the advantage of good heat stability. However, when the elevated temperature is higher than 380 °C, thermal cracking of PEG 6000 began. The differential scanning calorimetry and thermo gravimetric analyzer (DSC-TGA) analysis obtained in N_2 atmosphere (Fig. S1) displays that all the pyrolysis products are volatile, which probably are H_2, CH_4, CO and CO_2 [30,31]. In the process, Ni nanoparticles were exposed to the gas mixture. Under heating conditions, hydrocarbon decomposed and carbon atoms dissloved into Ni to form a solid solution. During the cooling down process, carbon atoms diffused out from the Ni-C composites and formed graphene films [32]. The infra-red spectra of PEG 6000 and the as-prepared TiO_2/G sample in Fig. S2 shows that all the characteristic peaks assigned to PEG 6000 had disappeared after the pyrolysis carbonization. Simultaneously, the TiO_2 nanotubes were converted from the amorphous phase to the crystalline phase during the heating process. Ni in the as-prepared TiO_2/Ni/G specimen were dissolved in 3 M HCl solution to yield a TiO_2/G specimen (Fig. 1c).

2.2.2. $TiO_2/G/Cu_2O$ mesh

The TiO_2/G mesh was plated with Cu particles in 10 mM $CuSO_4$ solution by applying a rectangular potential pulsed mode in a three-electrode system with the TiO_2/G mesh, a platinum wire, and a saturated calomel electrode as working, auxiliary, and reference electrodes, respectively. For pulsed electrodeposition, during each pulse, a potential of −2.0 V was applied for 0.2 s, followed by a potential of −0.1 V for 2 s at 25 °C. The number of consecutive pulse sequences was 80. The maximum pulsed electrodeposition current was -2.0×10^{-2} A/cm^2. After electrodeposition, the as-prepared TiO_2/G/Cu was anodized at 0.5 V for 0.5 h in 1 M NaOH solution. Anodization was carried out at 25 °C by using a two-electrode electrochemical cell with a Pt counter electrode.

2.3. Characterization and optical determination of $TiO_2/G/Cu_2O$ mesh

The morphologies of the resulting $TiO_2/G/Cu_2O$ mesh arrays were characterized by a field emission scanning electron microscopy (Nova NanoSEM 450, Holland). Transmission electron microscopy (TEM) images were obtained using a JEM 3010 (JEOL, Tokyo, Japan) operating at 300 KV. The crystal structure of the catalyst was investigated using the X-ray diffractometer (XRD, M21X, MAC Science Ltd., Japan) with Cu Ka radiation (λ = 0.15406 nm). UV–vis diffuse reflectance spectra (DRS) was conducted on a U-3900H spectrophotometer (Hitachi, Japan) equipped with a La-bsphere diffuse reflectance accessory within the 270–800 nm range, using $BaSO_4$ as a reflectance reference.The photoluminescence (PL) emission spectra were obtained usi-ng F-7000 fluorescence spectrophotometer (Hitachi, Japan). X-ray photoelectron spectroscopy (XPS) analyses of the specimen were carried out in an ultrahigh vacuumchamber with a pressure of 2×10^{-9} mbar at room temperature (Thermo Fisher Scientific, ESCALAB 250).

2.4. Photoelectrocatalysis on $TiO_2/G/Cu_2O$ mesh and analytical procedures

Photoelectrocatalytic removal of BPA with the $TiO_2/G/Cu_2O$ mesh was performed in a self-made photoelectrochemical reactor. The composite catalyst with an effective geometrical area of 4.0 cm^2 was placed in 160 mL of 15 mg L^{-1} BPA solution. A xenon lamp (CHF-XM35-500W, Beijing Trusttech. Co., Ltd.) was used to provide light with a radiation intensity of 85 mW/cm^2 as measured by a radiometer (OPHIR, Newport, USA). A DC power (Array 3646A, Taiwan, China) supplied electricity with a bias voltage of 0.5 V. Given the high adsorbability of $TiO_2/G/Cu_2O$, we presaturated $TiO_2/G/Cu_2O$ in 15 mg L^{-1} BPA solution for 45 min in the dark. After varied irradiation times, BPA solution was sampled to determine the absorbance at 276 nm by using a UV–vis spectrophotometer

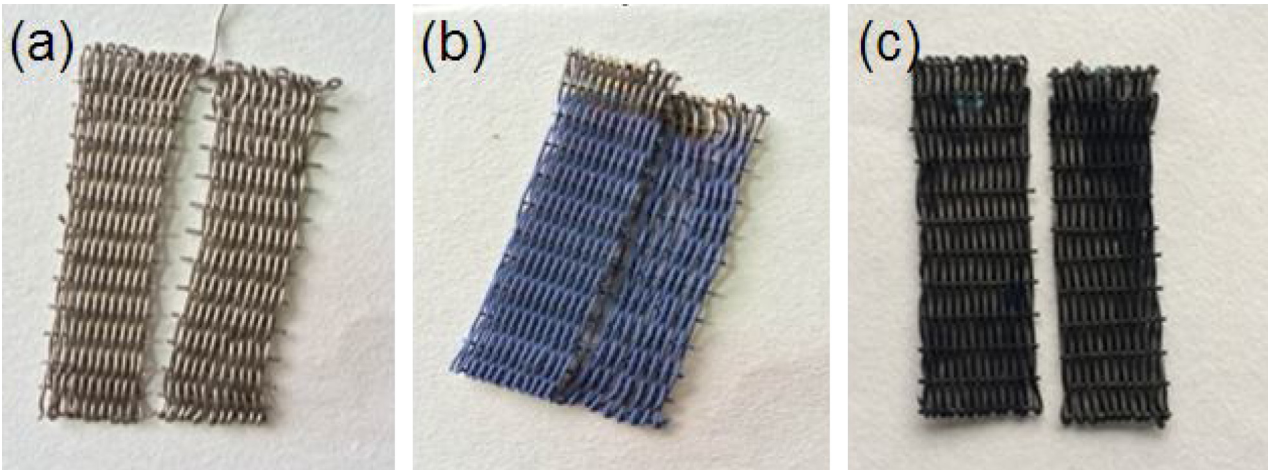

Fig. 1. Digital pictures of (a) Ti mesh withgeometrical size (1 cm × 5 cm), (b) TiO_2 NT arrays prepared by electrochemical anodization, (c) the as-prepared TiO_2/G mesh.

(U-3900H, Hitachi, Japan). Intermediate products in aqueous solution were identified using an Agilent 1100 series high-performance liquid chromatography/mass spectrometry detector (HPLC/MSD Trap/VL). The active oxidants involved in the photoelectrocatalysis is captured and identified by adding specific scavengers: tBuOH was employed for hydroxyl radicals, and EDTA-2Na was used to remove the contribution of holes, and nitroblue tetrazolium (NBT) was selected for deplete the superoxide radicals [33,34]. The concentrations of the scavengers were selected based on the experimental results and by referring the literature [33,34].

All analyses were carried out for a minimum of three replicates, and average values were reported.

3. Results and discussion

3.1. Morphology and structure characterization of the photocatalysts

The SEM images in Fig. 2 presents the morphologies of the TiO_2 nanotubes/Ti wire under varied magnification. The diameter of the Ti wire is about 600 μm, and the TiO_2 nanotubes are 3 μm in length, 120 nm in pore size and 15 nm in wall thickness. The SEM images of the as-prepared TiO_2/G nanotube arrays and the TiO_2/G/Cu_2O composite nanotube arrays are shown in Fig. 3. As shown in Fig. 3a, the oriented TiO_2 nanotubes are covered with graphene but retain the open top. Compared with the unmodified TiO_2 nanotubes in Fig. 2, the wall thickness of the nanotube increased and the gap between two nanotubes was filled. In particular, two separated nanotubes were connected by the graphene ribbons, which are marked by red arrows in Fig. 3b and c. Graphene exhibits superconductivity. In addition to the increased TiO_2 conductivity, graphene grown in situ on the TiO_2 nanotubes also rendered the nanotubes a stable and integrated substrate. The SEM images of TiO_2/G/Cu_2O in Fig. 3d and e displays that the Cu_2O particles are distributed on the top and side of the TiO_2 nanotube. The EDS spectrum and elemental analysis of the specimen are presented in Fig. 3f. The content of C, Ti, O and Cu in TiO_2/G/Cu_2O was supplied in Table S1.

The TEM images of the as-prepared TiO_2/G/Cu_2O nanowire arrays are shown in Fig. 4. The image in Fig. 4a demonstrates that the unmodified TiO_2 nanotubes are uniform and transparent. In Fig. 4b, the image of the TiO_2/G nanotubes is darker than that in Fig. 4a, suggesting that the graphene layer was coated on the TiO_2 nanotubes. Except for the general deposition on the external walls of the nanotubes, a special morphology of bamboo-shaped graphene inside the TiO_2 nanotubes was observed, as shown in Fig. 4c. Additional TEM images showing graphene with similar structures are provided in Fig. S3. The formation mechanism is summarized as follows. PEG6000 is a stable compound under general conditions. When the temperature in the tube furnace exceeds 380 °C, thermal cracking of PEG6000 began. Every product generated from this cracking is volatile and can be adsorbed on the Ni-plated TiO_2 nanotubes. The Ni nanoparticles are uniformly electrodeposited on the external and inner walls of the TiO_2 nanotubes. The morphologies of the dispersed Ni nanoparticles are demonstrated in Fig. S4. PEG6000 molecular fragments containing carbon atoms which penetrated into the inner space of the nanotubes, underwent catalytic decomposition over the Ni catalyst as evidenced by the dispersed Ni nanoparticles in the internal space of the TiO_2 nanotubes. During the growth of the graphene, morphology of the Ni nanoparticles changed constantly but remained metallic and crystalline. Due to the strong wall stress of the nanotubes as well as the deformation of the Ni particle by heat [35], the bamboo knots of the graphene sheets were preferentially formed inside the TiO_2 nanotubes. The bamboo-shaped graphene shown in Fig. 4c and Fig. S3 is typical when fabricated at low heating temperatures (600–650 °C) using Ni as catalyst [36,37]. Fig. 4d shows the top morphology of the graphene peeled from TiO_2 substrate. The graphene rings are replicas of the TiO_2 nanotubes. The TEM images in Fig. 4e show that the prepared Cu_2O particles present regular and cubical structure. Numerous small burrs with sharp corners were grown on the Cu_2O surface. During photocatalysis, the sharp corners and edges can function as active sites. Furthermore, Cu_2O particles are not stuffed but comprise small crystal cores, which will increase the specific surface area during the photocatalysis. Additional detailed TEM images illustrating the structure of Cu_2O are supplied in Fig. S5. High-resolution TEM image of Cu_2O in Fig. S5d shows a fringe spacing of 0.246 nm, which corresponds to the (1 1 1) plane of cubic-phase Cu_2O.

The crystalline phases of the TiO_2/G/Cu_2O composite were identified by XRD as shown in Fig. 5a. Only anatase phase of TiO_2 was detected. Anatase phase of TiO_2 exhibited higher photocatalytic activity than rutile and brookite phases. Compared with the intense TiO_2 peaks, graphitic carbon peak at $2\theta = 25.6°$ was detected which is very weak. As a powerful and more surface-sensitive technique than XRD [38], Raman spectroscopy was conducted to investigate the crystalline phases and the fine structure of the graphitic carbon. The Raman spectra of the TiO_2/G/Cu_2O specimens are shown in Fig. 5b. The band at 1320 cm^{-1} corresponds to carbon defect-induced Raman band (the D band). The band at 1589 cm^{-1} corresponds to the ordered graphitic structure (the G band) and the band at 2700 cm^{-1} corresponds to the graphene layer (the 2D band) [39,40]. The sharp and highly symmetric peak of the D band

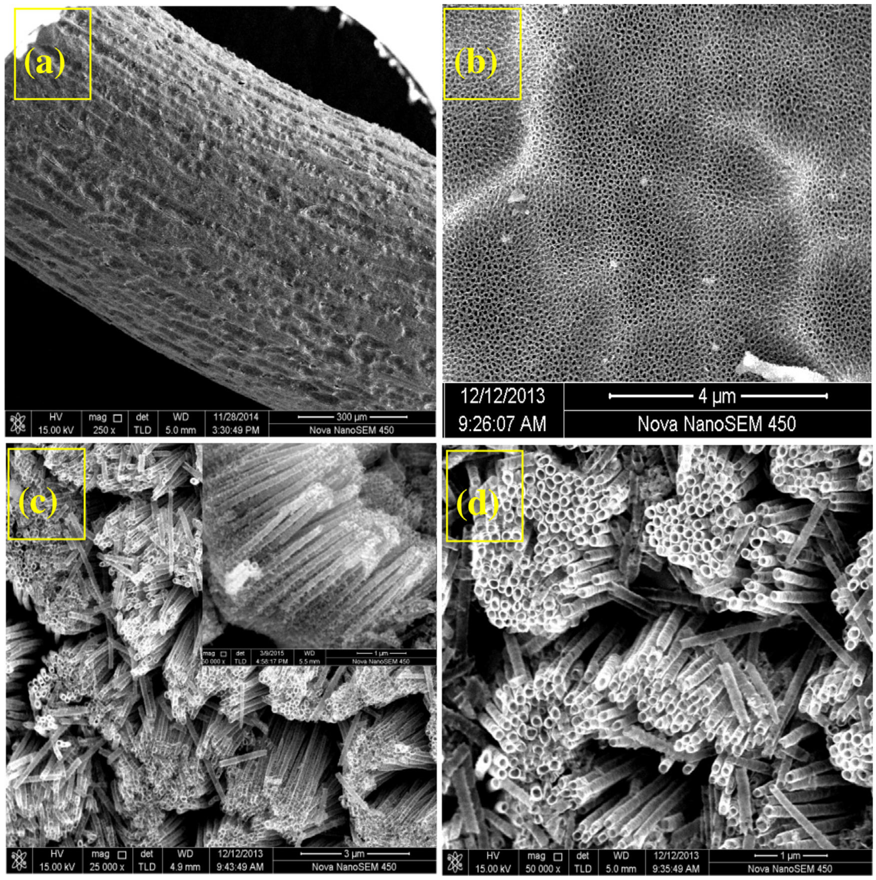

Fig. 2. SEM images in (a) and (b) with low magnification showing the whole morpholoies of TiO_2 nanotubes/Ti wire, SEM iamges in (c) and (d) with high magnification showing the detailed topologies of the TiO_2 nanotubes.

indicates a non-planar structures in the graphene. However, the value of I_D/I_G is lower than 1. This means that the defects in the graphene are relatively small [40,41]. Moreover, the Raman band at 635 cm^{-1} is assigned to the cuprous oxide and the bands at 199.8 and 399 cm^{-1} are attributed to the anatase phase of TiO_2 [42].

The XPS results in Fig. 6 show the characteristic peaks of Ti 2p (a) and O1s (b) which shifted to higher binding energies compared with the peaks of anatase TiO_2. In Fig. 6c, the N1s peak with low intensity is depicted indicating the content of N in the $TiO_2/G/Cu_2O$ is about 0.42 atomic%. The results suggest that the TiO_2 lattice was deformed due to N doping during the preparation of the TiO_2/G mesh in N_2 atmosphere. Nitrogen doping will result the defects in the doped TiO_2 making the N-doped TiO_2 sensitive to the visible light [43,44]. Furthermore, the XPS for C1s in TiO_2/G nanotubes and pure TiO_2 nanotubes was supplied in Fig. S6. There is no characteristic peak assigned to Ti–C band which is at 281.8 eV [44], which suggests that no carbon was doped in TiO_2.

The DRS spectra (Fig. 7a) of the TiO_2 nanotubes show that the sample absorbed UV light. However, the ultraviolet absorption intensity was enhanced and a red shift was observed for TiO_2/Cu_2O which means that the Cu_2O is beneficial in improving the response to visible light. TiO_2/G and $TiO_2/G/Cu_2O$ presented strong absorption toward light from 270 nm to 800 nm due to the strong light absorption of the black graphene. An inset in Fig. 7a shows the band gap of TiO_2/Cu_2O and TiO_2 nanotubes. The optical band gap, estimated by dropping a line from the maximum slope of the curve to the x-axis [45], is 3.06 eV for the TiO_2 nanotubes and 2.65 eV for the TiO_2/Cu_2O nanotubes, which are both smaller than that of bulk anatase TiO_2 (3.20 eV). Compared with that of TiO_2, the band gap is decreased, which indicates that the TiO_2/Cu_2O composite can adsorb the visible light.

In Fig. 7b, the ternary $TiO_2/G/Cu_2O$ photocatalyst exhibited the lowest photoluminescence (PL) intensity, whereas the pure TiO_2 showed the highest intensity. Because the PL of the semiconductor is due to the recombination of photogenerated electrons and holes. A weak PL intensity suggests that the $TiO_2/G/Cu_2O$ photocatalyst have low recombination. The PL spectra of TiO_2/G and TiO_2/Cu_2O illustrate that both graphene and Cu_2O improved the separation efficiency of photogenerated carriers. Graphene was more effective than Cu_2O and has higher transfer rate. These results show that the introduction of graphene between TiO_2 and Cu_2O will improve the separation of photogenerated holes and electrons.

3.2. Photoelectrocatalytic degradation of BPA over $TiO_2/G/Cu_2O$ mesh

In photocatalytic applications, a small bias voltage can reduce the interface charge-transfer resistance and effectively improve the separation efficiency of photogenerated hole–electron pairs. Experimental data show that the optimal bias value is 0.5 V (Supplementary data: Fig. S7). However, when the applied voltage was higher than 0.5 V, the photoelectrocatalytic activity was reduced. This is because a high voltage will make the width of the space-charge layer exceed the thickness of the photocatalyst that the charge will redistribute in the space-charge layer and the Helmholtz layer will increase [46,47]. So high voltage will not increase the photoelectrocatalytic activity but also increase the energy consumption

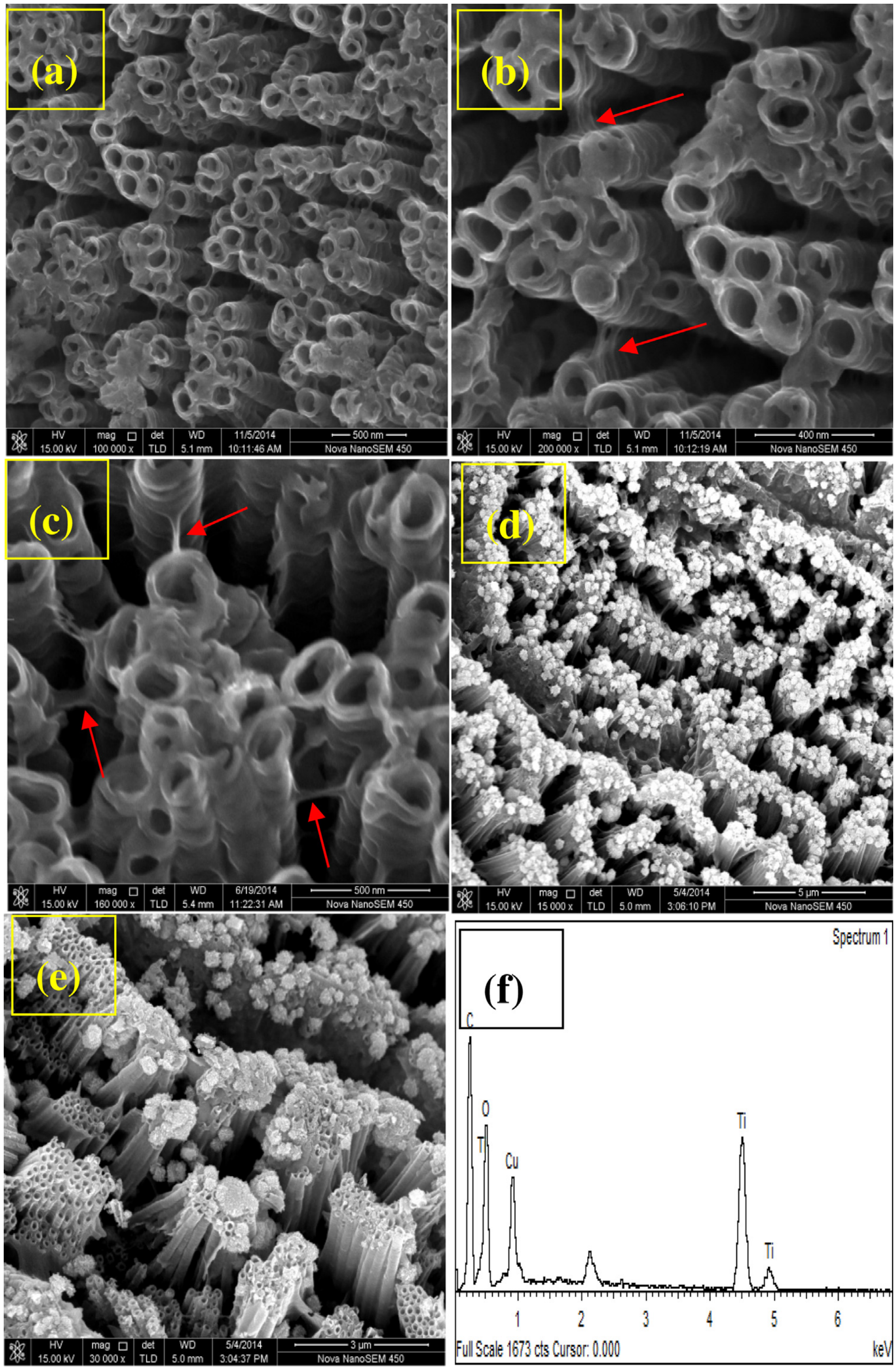

Fig. 3. (a) SEM image of the top surface of the TiO_2/G NT arrays, (b) and (c) SEM images showing thedetailed morphologies of TiO_2/G NT arrays, (d) and (e) SEM image showing Cu_2O crystals modified TiO_2/G NT arrays, and (f) EDS spectrum the TiO_2/G/Cu2O sample.

3.2.1. Influence of initial acidity on the degradation efficiency of BPA

Initial acidity can affect the oxidation potential and surface charge of the catalyst as well as the adsorption and dissociation of BPA and finally it determines the final catalysis efficiency [48]. The image in Fig. 8 displays the effect of pH (adjusted by HNO_3) on BPA removal efficiency. When pH was adjusted to 4.5, the optimal BPA removal efficiency was 92%. When pH was 7, 5 and 4, the removal efficiencies were 47%, 56% and 62%, respectively. When pH is less than 4, Cu_2O will be dissolved. When pH > 7, BPA will exist as an anion. At the same time, the electrostatic repulsion between BPA anions and the negatively charged surface of the photocatalyst will decrease the reaction probability of BPA [49], causing its degradation efficiency decreasing.

3.2.2. Degradation of BPA under variable conditions

As shown in Fig. 9a, BPA can not be degraded in the absence of the catalyst (curve 1). In the presence of the TiO_2/Cu_2O and

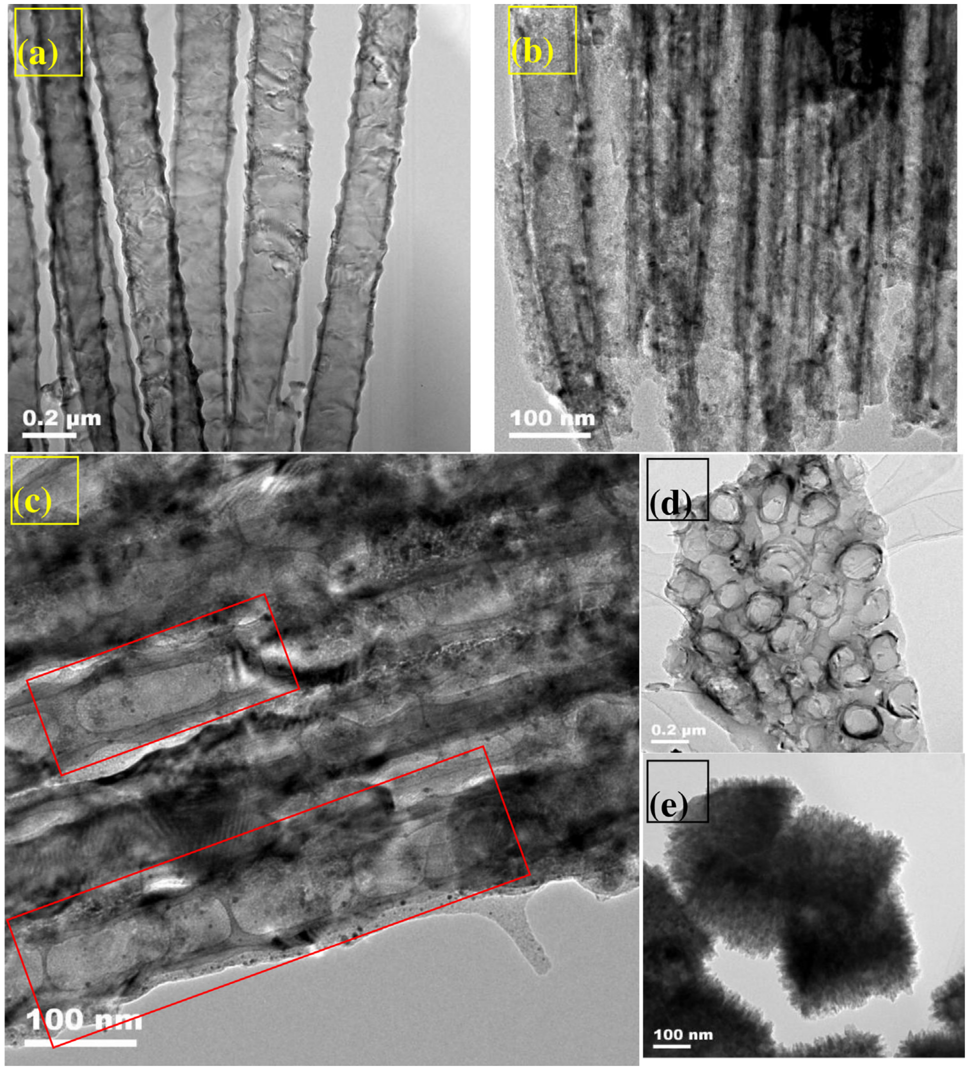

Fig. 4. (a) TEM image of unmodified TiO_2 nanotube arrays, (b) and (c) TEM images depicting the graphene morphologies of TiO_2/G NT arrays, (d) TEM image of top morphology of the graphene peeled from TiO_2 nanotubes, (e) TEM image of Cu_2O particles.

TiO_2/G/Cu_2O mesh, the obtained photodegradation efficiencies were 25% (curve 2) and 48% (curve 3), respectively. The results demonstrate that the TiO_2/G/Cu_2O mesh efficiently removed BPA under visible light. The enhanced performance can be attributed to the ternary photocatalyst–mediator–photocatalyst structures [50,51]. To obtain higher BPA degradation efficiency, a bias voltage (0.5 V) was applied. The photoelectrodegradation efficiency of BPA was 64% (curve 4). This is 16% higher than the pure photocatalytic degradation process. In order to improve the photoelectrodegradation efficiency, 50 mM H_2O_2 was added into the BPA solution as a co-catalyst because more hydroxyl radicals can be produced by the breakage of H_2O_2 [52,53]. The optimal removal efficiency of BPA was improved to 92% (curve 5) in the investigated time scale.

When the light source without filtering out the UV lights was increased to be 100 mW/cm^2 by improving the output power of the Xenon lamp. The corresponding results were provided in Fig. 9b. As the plots shown, the degradation efficiency of BPA under the UV–vis light was significantly improved due to strong photo energy from the UV light. Both TiO_2 and Cu_2O were excited by photo and generated active radicals to oxidize the BPA. The highest degradation efficiency was still achieved on TiO_2/G/Cu_2O assisted by bias voltage in the presence of H_2O_2 and 100% removal of BPA can be achieved in 90 min.

3.3. Photoelectrocatalytic mechanism and intermediates during the photoelectrodegradation process.

In this system, p-type Cu_2O and n-type TiO_2 were connected by the graphene, which seems like a p–n junction with Cu_2O particle being positive electrode, TiO_2 nanotube being negative electrode and graphene as external circuit with low contact resistance. As reported by Iwashina et al. and Iwase et al. [50,51]., the graphene interface is a crucial factor in ensuring a continuous flow of electrons between the electron source and the target photocatalyst. In TiO_2/G/Cu_2O, the electrons from TiO_2 CB directly recombine with the holes from Cu_2O VB when they go through the graphene, thus leaving holes in TiO_2 VB and electrons in Cu_2O CB. Although the TiO_2 is shielded by the graphene, the holes in TiO_2 VB can transfer onto the graphene and oxidize the adsorbed water there to produce the hydroxyl radicals [54]. The electrons in Cu_2O CB can react with the adsorbed oxygen and also generate hydroxyl radicals through a series of reactions shown as Scheme 1.

To reveal the photocatalytic mechanism further, the main oxidative species involved in the degradation of BPA are detected through controlled experiments using tBuOH as hydroxyl radical scavenger, EDTA-2Na as holes scavenger, and NBT as scavenger for superoxide radicals. As depicted in Fig. 10, after the introduction of the

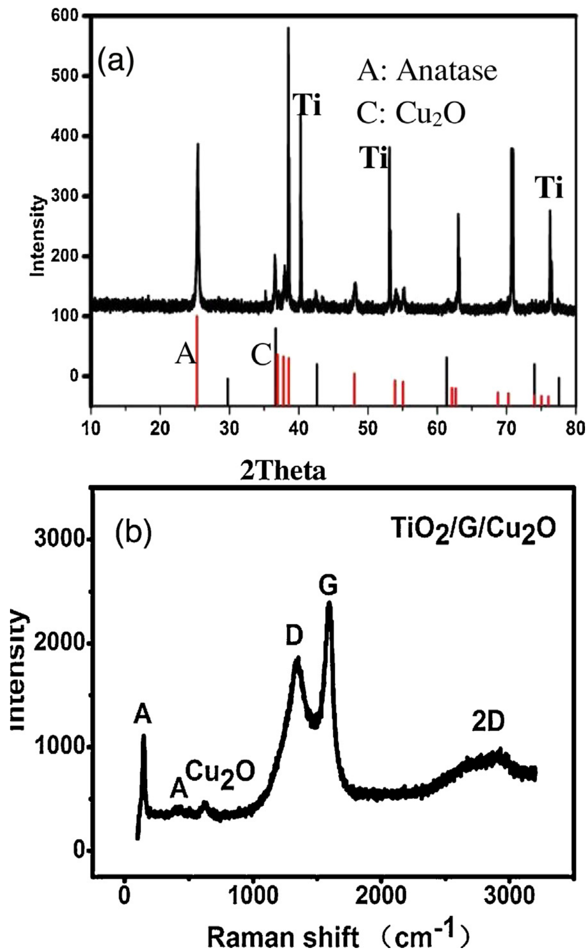

Fig. 5. (a) XRD pattern and (b) Raman spectrum of TiO_2/G/Cu_2O mesh.

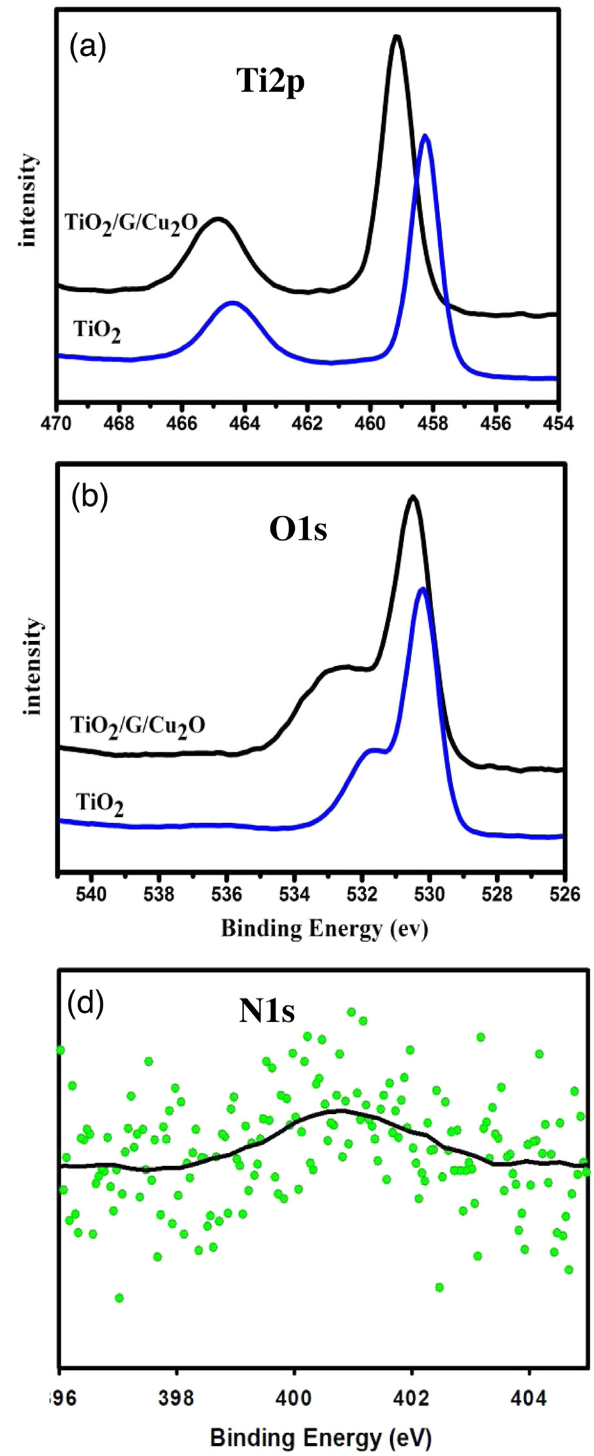

Fig. 6. High-resolution XPS spectra: (a) Ti 2p, (b) O1s, and (c) N1s of TiO_2 specimen.

scavengers, the degradation of BPA was restrained with EDTA-2Na showing the highest impact. Once EDTA-2Na was introduced, even only 0.5 mM in the BPA solution, the degradation was markedly restrained. When 1 mM EDTA-2Na was added, almost no BPA can be removed. As known, EDTA-2Na has a high chelating property. As a result, once there is EDTA-2Na in the solution, all the active sites such as metal ions on the photocatalyst surface can be occupied, the h^+—OH or e^-—O bonds can not be formed [55], resulting in no active species such as hydroxyl radicals or superoxide radicals being produced. Consequently, the declined photocatalytic efficiency is obtained due to the invalid h^+ and the lack of superoxide radicals which final product is still hydroxyl radical [53,55,56]. As for tBuOH and NBT, both of them can result in the decrease in removing BPA. However, the slight degradation of BPA was still carried out in the presence of tBuOH or NBT. That is because that the scavenger is ready to capture the active species dispersed in solution [57] while those adsorbed on the photocatalyst surface can survive to oxidize the adsorbed BPA molecules. Furthermore, since NBT is specific for superoxide radicals, the hydroxyl radicals from h^+ and the surviving superoxide radicals on the TiO_2/G/Cu_2O surface can still act in BPA removal, which causes the slightly higher degradation efficiency in comparison with that achieved in tBuOH medium. Considering the above experimental results, it is deduced that the hydroxyl radicals are the active species for attacking the BPA molecules.

The intermediate products during the BPA degradation and the corresponding structural formulas were identified through HPLC-MS as shown in Fig. 11. Except for the BPA peak at m/z 228, only three main peaks were observed at m/z 110.9, 108 and 132.9, respectively. They are corresponding to benzoquinone, p-hydroquinone and 4-isopropenylphenol, respectively (Supplementary data: Fig. S8). The HPLC chromatogram at 30 min depicts the decrease in the peak intensity of BPA (I) and an increase of the intensity of the intermediate products (peaks II, III and IV in the chromatogram). As the process proceed, the intensity of the intermediates decreased. The HPLC chromatogram obtained at 180 min shows no BPA, p-hydroquinone and 4-isopropenylphenol, but only a small amount of benzoquinone as shown in Fig. 11. The benzoquinone can be totally degraded without generating any further toxic products. The behavior of active species during BPA degrada-

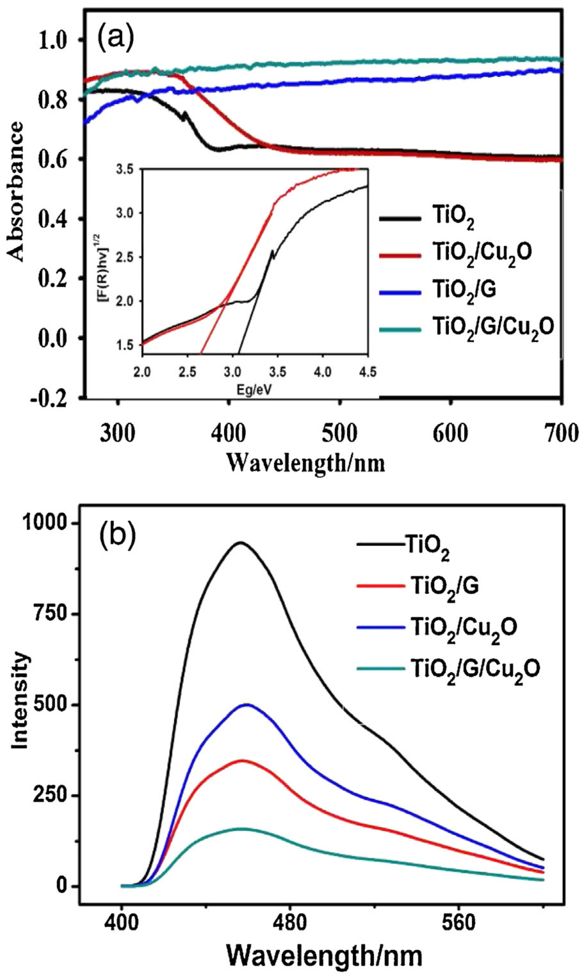

Fig. 7. (a) UV–vis diffuse reflectance spectra of TiO_2, TiO_2/Cu_2O, TiO_2/G, and $TiO_2/G/Cu_2O$ with an inset showing the band gap of TiO_2 and TiO_2/Cu_2O nanotubes, (b) fluorescence emission spectra of TiO_2, TiO_2/Cu_2O, TiO_2/G and $TiO_2/G/Cu_2O$.

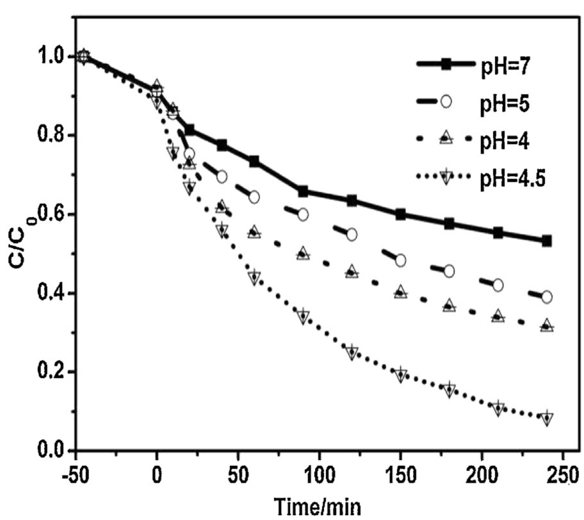

Fig. 8. Influence of initial acidity on photoelectrocatalysis degradation of BPA V_{total} = 160 mL, $S_{catalyst}$ = 4.0 cm^2, light source: Xe lamp, 85 mW/cm^2, power source: DC power, 0.5 V.

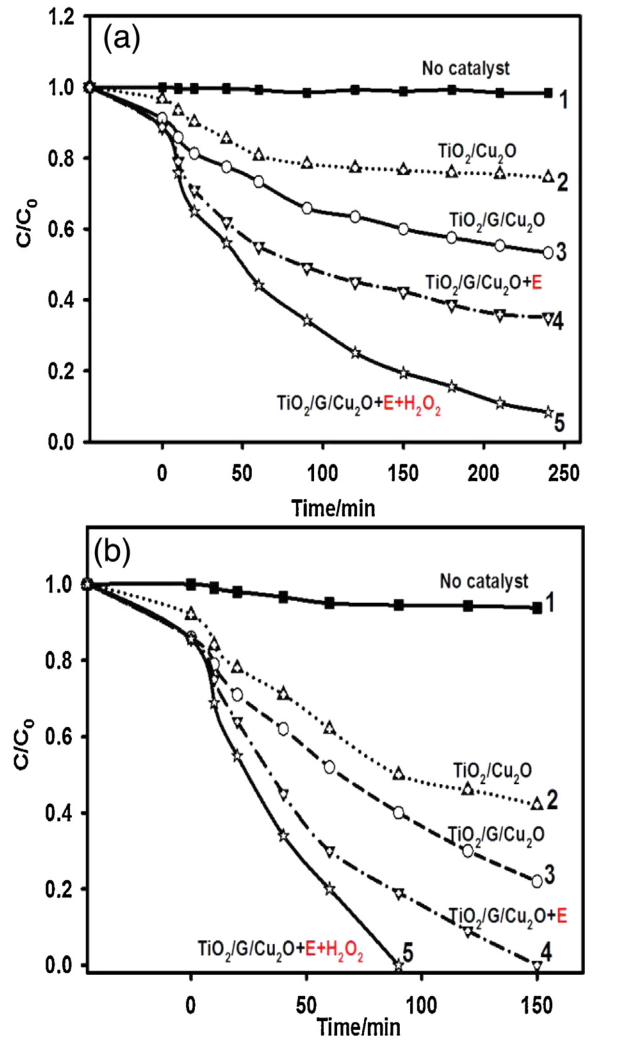

Fig. 9. Degradation of BPA under 85 mW/cm^2,visible light (a) and 100 mW/cm^2 UV–vis light (b) in control experiments under different conditions: no catalyst (curve 1), TiO_2/Cu_2O mesh (curve 2), $TiO_2/G/Cu_2O$ mesh (curve 3), $TiO_2/G/Cu_2O$ mesh +E (curve 4), $TiO_2/G/Cu_2O$ mesh +E +50 mM H_2O_2 (curve 5). V_{total} = 160 mL, $S_{catalyst}$ = 4.0 cm^2, light source: Xe lamp, power source: DC power, 0.5 V. *E* represents that there is a bias potential of 0.5 V.

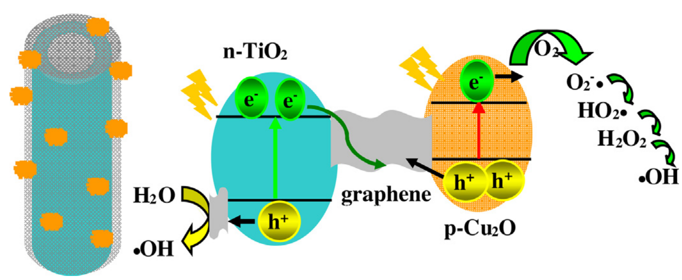

Scheme 1. Schematic diagrams illustrating the construction and the possible transfer behaviors of the photogenerated holes and electrons in$TiO_2/G/Cu_2O$ interface.

tion and the degradation pathway of BPA as well as intermediate generation are illustrated as below.

Eqs. (1) and (2) depicted that both Cu_2O and N doped TiO_2 can be excited by visible light to produce hole–electron pairs. The free electrons was excited into the TiO_2 CB, leaving holes in the VB of TiO_2. In Eq. (3), the electrons from TiO_2 CB recombine with the holes from the VB of Cu_2O when they across the inserted graphene layer. After that, the holes from TiO_2 VB migrate to the graphene surface

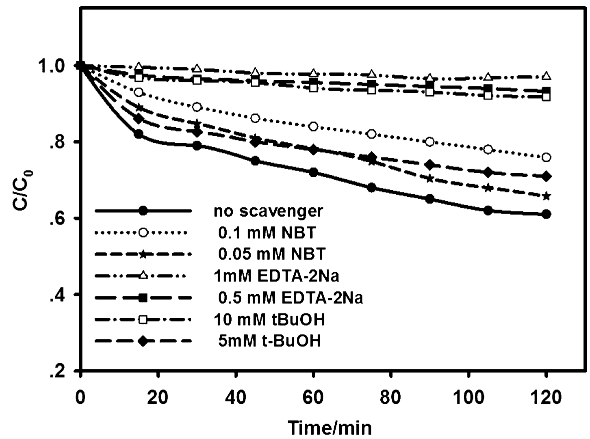

Fig. 10. Photocatalytic degradation of BPA over $TiO_2/G/Cu_2O$ mesh in the presence of scavengers for active species: EDTA-2Na for h^+, tBuOH for $^{\bullet}OH$, and NBT for $^{\bullet}O_2$ radicals mg/L, $S_{catalyst}$ = 4.0 cm^2, pH 4.5, no H_2O_2, no bias potential.

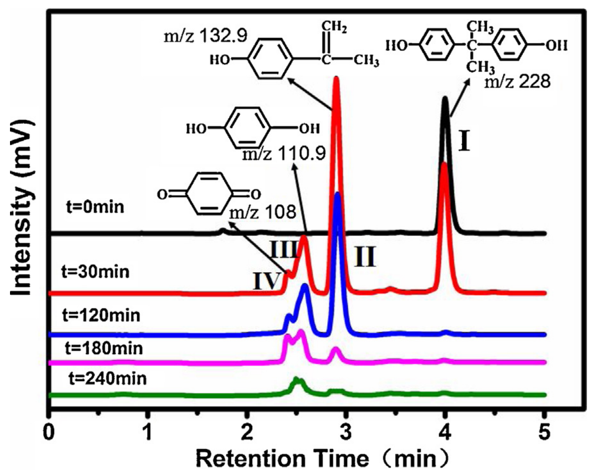

Fig. 11. Evolution of HPLC chromatograms during the degradation of BPA.

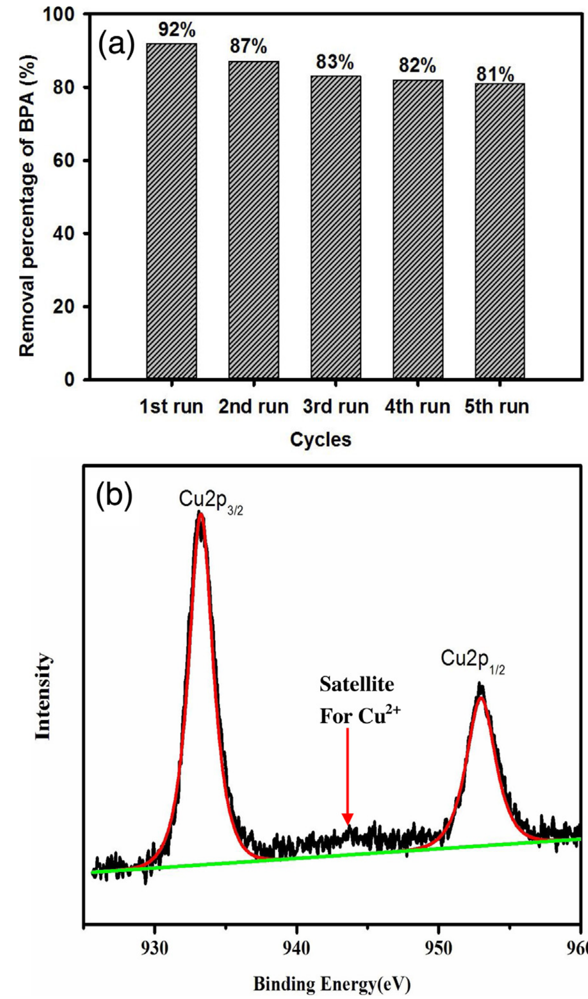

Fig. 12. (a) Recycling properties of the $TiO_2/G/Cu_2O$ mesh, (b) XPS spectrum of Cu 2p in the $TiO_2/G/Cu_2O$ after multiple use in the photoelectrocatalysis.

and oxidize the adsorbed H_2O to be $^{\bullet}OH$ radicals (Eqs. (4), (5)). The generation of $^{\bullet}OH$ radicals by the electrons in Cu_2O CB is depicted in Eqs. (6)–(10) [53]. The process includes formations of the $^{\bullet}O_2^-$ (Eq. (6)), $HO_2^{\bullet}$ (Eq. (7)). H_2O_2 is generated through the termination reactions between $HO_2^{\bullet}$ radicals in Eq. (8). Then H_2O accepts the electrons and reacts with H^+ to generate $^{\bullet}OH$ radicals. From Eqs. (1) to (9), we can see that the hydroxyl radicals are the main active species for BPA degradation (Eq. (10)).

$$TiO_2 + h\nu(\text{vis}) \rightarrow TiO_2(e^-{}_{CB} + h^+{}_{VB}) \quad (1)$$

$$Cu_2O + h\nu(\text{vis}) \rightarrow Cu_2O(e^-{}_{CB} + h^+{}_{VB)} \quad (2)$$

$$TiO_2(e^-{}_{CB}) + \text{graphene} + Cu_2O(h^+{}_{VB}) \rightarrow \text{recombination of } e^- - h^+ \quad (3)$$

$$TiO_2(h^+{}_{VB}) + \text{graphene} \rightarrow TiO_2 + \text{graphene}(h^+{}_{VB}) \quad (4)$$

$$\text{graphene}(h^+{}_{VB}) + OH_{ads} \rightarrow {}^{\bullet}OH + \text{graphene} \quad (5)$$

$$Cu_2O(e^-{}_{CB}) + O_2 \rightarrow {}^{\bullet}O_2{}^- + Cu_2O \quad (6)$$

$$4{}^{\bullet}O_2{}^- + H^+ \rightarrow HO_2{}^{\bullet} \quad (7)$$

$$HO_2{}^{\bullet} + HO_2{}^{\bullet} \rightarrow H_2O_2 + O_2 \quad (8)$$

$$H_2O_2 + ne^- + H \rightarrow {}^{\bullet}OH + H_2O \quad (9)$$

$$OH + BPA \rightarrow \text{intermediates} \rightarrow CO_2 + H_2O \quad (10)$$

Based on the HPLC and MS results, intermediate II, III and IV are formed during the process as shown in Scheme 2. So the degradation pathway of BPA are illustrated. First, the quaternary carbon atom in BPA are attacked by the $^{\bullet}OH$ radicals. Then the attacked intermediate was cleaved to phenol and 4-isopropenylphenol (II). The cleavage of the middle carbon atom of the BPA under attacking of $^{\bullet}OH$ radicals is also proposed by Subagio et al. [58]. and other researchers [59–61] Then these intermediate species of phenol and 4-isopropenylphenol were further transformed to p-hydroquinone (III) and 4-hydroxyacetophenone through hydroxylation reactions. The 4-hydroxyacetophenone will be further transformed to p-hydroquinone (III) The p-hydroquinone (III) will react with the oxygen radical to produce benzoquinone (IV). Then the benzoquinone can be easily oxidized by radicals to generate maleic and oxalic acids, which can be oxidized to carbon dioxide.

4.1. Stability of the $TiO_2/G/Cu_2O$ mesh

Fig. 12(a) shows the stability of the $TiO_2/G/Cu_2O$ mesh after being used 5 times under the same conditions. As the data shown, the degradation efficiency of BPA decreased by 11% after the 5th application, the photocatalyst possesses good stability and keeps well photoelectrocatalytic activity in BPA removal under the visible light. XPS spectra obtained on the $TiO_2/G/Cu_2O$ after multiple use in Fig. 12(b) shows that the characteristic peak of a slight satellite peak at about 944 eV assigned to Cu(II) [62]. The oxidation of

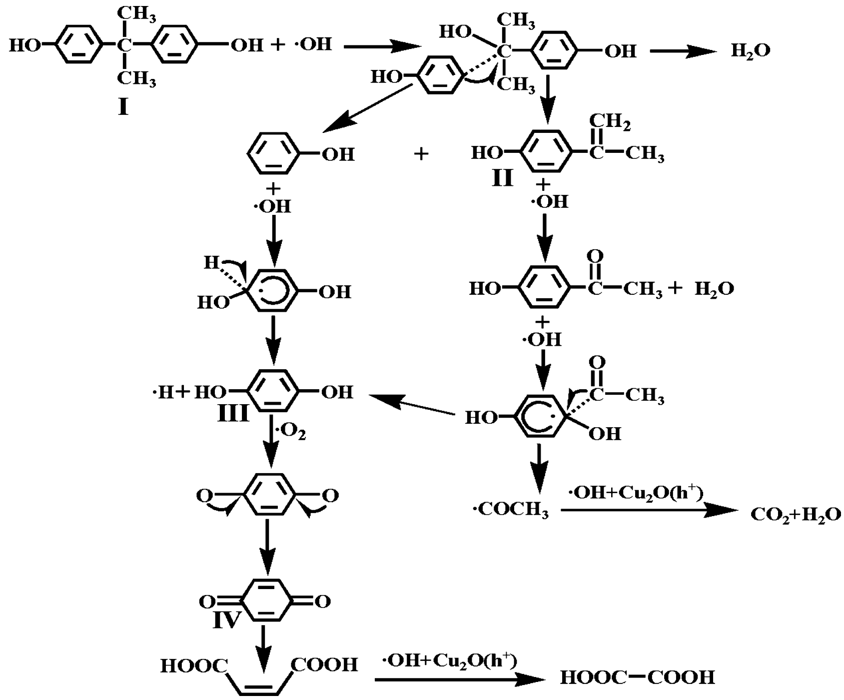

Scheme 2. Possible degradation pathway of BPA during the photoelectrocatalytic process.

Cu(I) might be caused by reacting with the adsorbed oxygen during the photoelectrocatalysis with taking the TiO_2/G/Cu_2O as anode. However, Cu_2O can be reborn by being anodized in the fresh NaOH solution. The related reactions are listed below [63,64].

$$Cu^{2+} + 2OH^- \rightarrow Cu(OH)_2 \quad (11)$$

$$Cu(OH)_2 \rightarrow Cu_2O + H_2O \quad (12)$$

5. Conclusions

A TiO_2/G/Cu_2O mesh was facilely fabricated by annealing crystalline TiO_2 nanotube arrays under carbon atmosphere and subsequently cubic Cu_2O particles was coating with fine burrs deposited on their surface. The ternary TiO_2/G/Cu_2O catalyst shows good photoelectrocatalytic activity for the degradation of BPA under visible light irradiation. This can be ascribed to the high conductive and interconnected three-dimensional channels inside the TiO_2/G/Cu_2O mesh. Bamboo-shaped graphene was formed in the TiO_2 nanotubes under catalysis by Ni nanoparticles because of strong wall stress inside the nanotubes. All fabrication processes of TiO_2/G/Cu_2O were conducted under mild conditions, which can be easily controlled and environment friendly. As the mesh is a solid, soft and conductive substrate, it can be conveniently incorporated as a system core in an apparatus, suggesting a promising application future.

Acknowledgments

This work is financially supported by the National Natural Science Foundation of China (Grants 51272099, 51478214, 51238002, 51468044), Department of Education fund of Jiangxi Province (Grant GJJ14516), Science and technology major project of Jiangxi Province (Grant 20124ABG04102) and National Natural Science Foundation of Jiangxi Province (20122BAB203003) are acknowledged.

Appendix A. Supplementary data

Supplementary data associated with this article can be found, in the online version, at http://dx.doi.org/10.1016/j.apcatb.2015.10.023.

References

[1] Y.Q. Huang, C.K. Wong, J.S. Zheng, H. Bouwman, R. Barra, B. Wahlström, L. Neretin, M.H. Wong, Environ. Int. 42 (2012) 91–99.
[2] L. Yu, C.P. Wang, X.H. Ren, H.W. Sun, Chem. Eng. J. 252 (2014) 346–354.
[3] J. Jackson, R. Sutton, Sci. Total Environ. 405 (2008) 153–160.
[4] J. Sánchez-Avila, J. Bonet, G. Velasco, S. Lacorte, Sci. Total Environ. 407 (2009) 4157–4167.
[5] M.J. Gómez, M.J. Martínez-Bueno, S. Lacorte, A.R. Fernández Alba, A. Agüera, Chemosphere 66 (2007) 993–1002.
[6] H.M. Kuch, K. Ballschmiter, Environ. Sci. Technol. 35 (2001) 3201–3206.
[7] S. Flint, T. Markle, S. Thompson, E. Wallace, J. Environ. Manage. 104 (2012) 19–34.
[8] G. Liu, J. Ma, X. Li, Q. Qin, J. Hazard. Mater. 164 (2009) 1275–1280.
[9] R.T. Zoeller, R. Bansal, C. Parris, Endocrinology 146 (2005) 607–612.
[10] M.V. Maffini, B.S. Rubin, C. Sonnenschein, A.M. Soto, Mol. Cell Endocrinol. 254 (2006) 179–186.
[11] X.P. Wang, T.T. Lim, Appl. Catal. B: Environ. 100 (2010) 355–364.
[12] M. Wright-Walters, C. Volz, E. Talbott, D. Davis, Sci. Total Environ. 409 (2011) 676–685.
[13] A.F. Fleisch, R.O. Wright, A.A. Baccarelli, J. Mol. Endocrinol. 49 (2012) 61–67.
[14] T. Geens, D. Aerts, C. Berthot, J.P. Bourguignon, Food Chem. Toxicol. 50 (2012) 3725–3740.
[15] J.Y. Hu, T. Aizawa, S. Okubo, Environ. Sci. Technol. 36 (2002) 1980–1987.
[16] M.C.G. Antunes, S. Pinto, F.G. Braga, J. Silva, Chem. Ecol. 28 (2012) 141–152.
[17] L. Joseph, Q. Zaib, I.A. Khan, N.D. Berge, Y.G. Park, N.B. Saleh, Y. Yoon, Water Res. 45 (2011) 4056–4068.
[18] Y. Kimura, M. Yamamoto, R. Shimazaki, A. Kashiwada, K. Matsuda, K. Yamada, J. Appl. Polym. Sci. 124 (2012) 796–804.
[19] Q. Xie, J. Xie, Z. Wang, D. Wu, Z. Zhang, H. Kong, Micropor. Mesopor. Mater. 179 (2013) 144–150.
[20] J.W. Ng, X.P. Wang, D.D. Sun, Appl. Cata. B: Environ. 110 (2011) 260–272.
[21] H. Melcer, G. Klecka, Water Environ. Res. 83 (2011) 650–666.
[22] B. Seyhi, P. Drogui, G. Buelna, J.F. Blais, Sep. Sci. Technol. 87 (2012) 101–109.
[23] (a) M.R. Hoffmann, S.T. Martin, W. Choi, D.W. Bahnemann, Chem. Rev. 95 (1995) 69–96;
(b) X. Chen, S.S. Mao, Chem. Rev. 107 (2007) 2891–2959.
[24] (a) U.G. Akpan, B.H. Hameed, J. Hazard. Mater. 170 (2009) 520–529;
(b) S.G. Kumar, L.G. Devi, J. Phys. Chem. A 115 (2011) 13211–13241.
[25] (a) C.A. Grimes, G.K. Mor, TiO_2 nanotube Arrays: Synthesis, Properties, and Appli-cations, Springer, New York, 2009;

(b) I. Paramasivam, H. Jha, N. Liu, P. Schmuki, Small 8 (2012) 3073–3103; (c) A.E.R. Mohamed, S. Rohani, Energy Environ. Sci. Technol. 4 (2011) 1065–1086.
[26] J. Shang, S.D. Xie, T. Zhu, J. Li, Environ. Sci. Technol. 41 (2007) 7876–7880.
[27] F.M.M. Paschoal, G. Pepping, M.V.B. Zanoni, M.A. Anderson, Environ. Sci. Technol. 43 (2009) 7496–7502.
[28] Q.Y. Liu, C.S. Xie, H.Y. Li, H. Chen, Y. Liao, D.W. Zeng, Appl. Catal. B: Environ. 102 (2011) 157–162.
[29] T.T. Li, X.Y. Li, Q.D. Zhao, Y. Shi, W. Teng, Appl. Cata. B: Environ. 156–157 (2014) 362–370.
[30] C.W. Huang, Y.Y. Li, J. Phys. Chem. B 110 (2006) 23242–23246.
[31] L.L. Cao, Z.Q. Li, G.L. Fan, L. Jiang, D. Zhang, W.-J. Moon, Y.-S. Kin, Carbon 50 (2012) 1057–1062.
[32] Y. Zhang, L.Y. Zhang, C.W. Zhou, Acc. Chem. Res. 46 (2013) 2329–2339.
[33] Y. Li, S.L. Luo, Z.D. Wei, D.S. Meng, M.Y. Ding, C.B. Liu, Phys. Chem. Chem. Phys. 16 (2014) 4361–4368.
[34] L. Zhang, W.Z. Wang, S.M. Sun, Y.Y. Sun, E.P. Gao, Z.J. Zhang, Appl. Catal. B: Environ. 148–149 (2014) 164–169.
[35] M. Lin, J.P.Y. Tan, C. Boothroyd, P.L. Kian, S.T. Eng, L.F. Yong, Nano Lett. 7 (2007) 2234–2238.
[36] M. Moseler, F. Cervantes-Sodi, S. Hofmann, G. Csányi, A.C. Ferrari, ACS Nano 4 (2010) 7587–7595.
[37] L. Sun, F. Banhart, A.V. Krasheninnikov, J.A. Rodriguez-Manzo, M. Terrones, P.M. Ajayan, Science 312 (2006) 1199–1202.
[38] N. Lu, X. Quan, J. Li, S. Chen, G.H. Chen, J. Phys. Chem. C 111 (2007) 11836–11842.
[39] L.X. Yang, S.L. Luo, S.H. Liu, Q.Y. Cai, J. Phys. Chem. C 112 (2008) 8939–8943.
[40] A.C. Ferrari, J.C. Meyer, V. Scardaci, K.S. Novoselov, S. Roth, Phys. Rev. Lett. 97 (2006) 187401–187404.
[41] A.C. Ferrari, D.M. Basko, Nat. Nanotech. 8 (2013) 235–245.
[42] T. Ohsaka, F. Izumi, Y. Fujiki, J. Raman Spectrosc. 7 (1978) 321–324.
[43] J. Wang, D. Nyago Tafen, J.P. Lewis, Z.L. Hong, A. Manivannan, M.J. Zhi, M. Li, N.Q. Wu, J. Am. Chem. Soc. 131 (2009) 12290–12297.
[44] X.B. Chen, B. Clemens, J. Am. Chem. Soc. 130 (2008) 5018–5019.
[45] N. Serpone, D. Lawless, R. Khairutdinov, J. Phys. Chem. 99 (1995) 16646–16654.
[46] B. Oran, J. Moser, M. Anderson, J. Phys. Chem. 94 (1990) 8720–8726.
[47] C.S. Chih, C.C. Tse, Ind. Eng. Chem. Res. 11 (1998) 4207–7214.
[48] L.X. Yang, W.S. Sun, S.L. Luo, Y. Luo, Appl. Catal. B: Environ. 156 (2014) 25–34.
[49] P. Kristense, K. Lindblom, E. Schmidt, J.E. Henze, Water Sci. Technol. 57 (2008) 1253–1256.
[50] A. Iwase, Y.H. Ng, Y. Ishiguro, A. Kudo, R. Amal, J. Am. Chem. Soc. 133 (2011) 11054–11057.
[51] K. Iwashina, A. Iwase, Y.H. Ng, R. Amal, A. Kudo, J. Am. Chem. Soc. 137 (2015) 604–607.
[52] L.J. Xu, J.L. Wang, Sci. Technol. Technol. 46 (2012) 10145–10153.
[53] Z.T. Hu, B. Chen, T.T. Lim, RSC Adv. 4 (2014) 27820–27829.
[54] Y.H. Tang, X. Hu, C.B. Liu, Phys. Chem. Chem. Phys. 16 (2014) 25321–25329.
[55] J. Schneider, M. Matsuoka, M. Takeuchi, J.L. Zhang, Y. Horiuchi, M. Anpo, D.W. Bahnemann, Chem. Rev. 114 (2014) 9919–9986.
[56] N. Lu, Y. Lu, F.Y. Liu, K. Zhao, X. Yuan, Y.H. Zhao, Y. Li, H.W. Qin, J. Zhu, Chemosphere 91 (2013) 1266–1272.
[57] Y. Lei, C.S. Chen, Y.J. Tu, Y.H. Huang, H. Zhang, Environ. Sci. Technol. 49 (2015) 6838–6845.
[58] D. Subagio, M. Srinivasan, M. Lim, T. Lim, Appl. Catal. B: Environ. 95 (2010) 414–422.
[59] A.O. Kondrakov, A.N. Ignatev, F.H. Frimmel, S. Brase, H. Horn, A.I. Revelsky, Appl. Cata. B: Environ. 160–161 (2014) 106–114.
[60] L. Yu, C.P. Wang, X.H. Ren, H.W. Sun, Chem. Eng. 252 (2014) 346–354.
[61] X.Y. Zhang, Y.B. Ding, H.Q. Tang, X.Y. Han, L.H. Zhu, N. Wang, Chem. Eng. 236 (2014) 251–262.
[62] P. Liu, E.J.M. Hensen, J. Am. Chem. Soc. 135 (2013) 14032–14035.
[63] D.P. Singh, N.P. Neti, A.S.K. Sinha, O.N. Srivastava, J. Phys. Chem. C 111 (2007) 1638–1645.
[64] E. Ko, J. Choi, K. Okamoto, Y. Tak, J. Lee, Chem. Phys. Chem. 7 (2006) 1505–1509.